MDPI

Article

Optimization of Submerged Breakwaters for Maximum Power of a Point-Absorber Wave Energy Converter Using Bragg Resonance

Sanghwan Heo and **Weoncheol Koo** *

Department of Naval Architecture and Ocean Engineering, Inha University, Incheon 22212, Republic of Korea;
sanghwan.heo@gmail.com
* Correspondence: wckoo@inha.ac.kr

Abstract: This study focused on optimizing the power generation of a heaving point-absorber wave energy converter (HPA-WEC) by integrating submerged breakwaters. An optimization analysis was conducted based on a framework developed in the authors' previous work, aiming to maximize the capture width ratio (CWR) by inducing Bragg resonance. Numerical simulations were conducted using a two-dimensional frequency domain boundary element method (FD-BEM) under irregular wave conditions. Advanced particle swarm optimization (PSO) was used for the optimization, with design variables that included the power take-off (PTO) damping coefficient, spring constant, and position and shape of the submerged breakwaters. The results showed that the CWR almost doubled when two breakwaters were used compared with the case without breakwaters. The CWR significantly increased, even with only one breakwater installed behind the WEC. A coastal stability analysis showed that installing two breakwaters provided the best performance, reducing the transmitted wave energy by approximately 25%. Furthermore, the CWR reached its maximum when the distance between the breakwater endpoints equaled the wavelength of the peak wave frequency, indicating the occurrence of Bragg resonance. This study underscores the potential of submerged breakwaters in enhancing power generation and coastal stability in the design of HPA-WECs.

Keywords: hydrodynamics; submerged breakwater; heaving point-absorber; wave energy converter; optimization analysis; numerical wave tank

check for updates

1. Introduction

The imperative for renewable energy sources has escalated, primarily driven by environmental concerns, including global warming. Among the various forms of renewable energy sources, wind, ocean wave, and solar energies stand out as particularly clean and vital options. These energy sources are increasingly pivotal in achieving zero emissions, an essential goal for mitigating the adverse effects of climate change and promoting environmental sustainability [1]. In particular, ocean wave energy has the highest energy density [2], and numerous types of wave energy converters (WECs) have been developed to extract energy from ocean waves [3]. Ocean wave energy acting on WECs is converted into electrical energy using power take-off (PTO) systems [4].

WECs can be classified according to their working principles, such as oscillating water columns, oscillating body systems, and overtopping systems [5]. This study considered the point-absorber (PA) concept, one of the oscillating body systems, because the PA can be scaled from small to large [6]. The PAs are called the WECs, which have relatively small characteristic dimensions compared with the wavelength, and harvest ocean wave energy by oscillating the PA body with single or multiple degrees of freedom (DoFs) [7,8]. PAs can be classified into one-body PAs and two-body PAs according to the viewpoint of the body geometry [7]. In general, a floating one-body PA generates electrical energy using the heave motion of the floating body and is called a heaving point-absorber (HPA). The period of the heave resonance of the floating body and the period of the incident wave must be

designed to be close to each other to increase the amount of the power production of an HPA-type WEC. A control strategy, such as a latching control, can be applied to maximize power production when the resonance period between the floating body and the incident wave is distant [9].

In nearshore areas, breakwaters can be built to resist wave energy [10]. Kim et al. [11] highlighted the significance of the crest depth in wave height attenuation around low-crested structures using a deep neural network model. Hwang et al. [12] examined the flow patterns, topographic changes, and sediment transport in a coastal area with submerged breakwaters through numerical simulations and field observations, highlighting the significant influence of incident wave direction on these phenomena, particularly under high-wave conditions such as typhoons, facilitating the design of efficient SBW arrangements. In particular, connecting a PTO system to a floating breakwater can reduce wave energy and produce electrical energy as a WEC [13,14]. Hydrodynamic analyses of breakwaters are mainly performed in a two-dimensional domain because breakwaters are installed long and parallel to the shoreline and have a constant cross-section.

Studies on HPA-WECs have predominantly assumed or restricted the WECs to vertical motion only. Ning et al. [15] examined the heave response amplitude operator (RAO) and capture width ratio (CWR) of a pile-restrained HPA-type WEC floating breakwater. They also analyzed the reflection, transmission, and dissipation coefficients. Zhao et al. [16] conducted a theoretical analysis in the frequency domain based on the linear potential theory for a pile-restrained HPA-type WEC floating breakwater. They conducted a parametric study of the shape of the WEC and the PTO damping coefficient. Shadman et al. [17] conducted a geometrical optimization analysis of an HPA-type WEC to maximize the capture width. Reabroy et al. [18] conducted experiments and CFD-based numerical analyses considering the interaction with an HPA-WEC installed in front of a fixed breakwater. They performed a comparative analysis of various geometric shapes of WEC. The results suggested that the Dolphin model had the best power production and hydrodynamic performance. Zhang et al. [14] conducted a CFD-based numerical analysis on an HPA-type WEC floating breakwater with various bottom shapes. The results suggested that a WEC can be helpful with coastal protection. Zhang et al. [19] analyzed the hydrodynamic performance of an HPA-WEC installed in front of a vertical wall using the eigenfunction expansion method in the frequency domain. Ahmed et al. [20] performed a time domain irregular wave analysis on various bulbous-bottomed HPA-WECs and presented new buoy shapes for optimal HPA-WECs. He et al. [21] conducted an optimization analysis using the differential evolution algorithm to maximize the power production performance of an HPA-WEC.

A notable limitation in these studies is the constraint of the WEC to vertical movement. This simplification neglects potential horizontal and rotational motions of the WEC, which are crucial for accurately evaluating the performance and stability of WECs in practical applications. Considering the multiple DoF motions of a WEC, it is essential to account for a mooring system to ensure station-keeping. Nguyen et al. [22] conducted experimental research, showing that the mooring-line tension in floating structures is significantly influenced by the wave direction. In particular, they observed peak tension when the lines aligned parallel to the wave propagation. Rossell et al. [23] conducted an experimental study on a circular pipe-shaped floating breakwater, considering vertical and inclined mooring systems. Guo et al. [24] performed smoothed-particle hydrodynamic (SPH) simulations to analyze the hydrodynamic performance of a floating breakwater considering taut, slack, and hybrid mooring systems. These studies suggested that the performance of a floating breakwater varies, depending on the type of mooring system and the location of the anchor point. Xu et al. and Qiao et al. [25,26] introduced various mooring-system designs for floating WECs.

The hydrodynamic performance of a floating structure or a vertical wall is affected by the submerged breakwater installed in front of the structure. Manisha et al. [27] analyzed the effects of submerged breakwaters or trenches of various shapes on reducing the wave

loads acting on a fixed floating bridge. Vijay et al. [28] performed a parametric analysis of external forces and ascertained the reflection and transmission coefficients acting on a fixed floating dock by considering the interactions between submerged breakwaters and the structure. Jiang et al. [29] analyzed the trends in the reflection, dissipation, and improvement enhancement coefficients caused by double- and triple-submerged breakwaters installed in front of a vertical wall. These studies aimed to reduce the wave loads acting on the rear of the structure due to reflected waves and dissipated wave energy by submerged breakwaters. Heo et al. [30] performed an optimization analysis on the shape and position of a submerged breakwater. The results suggest that the magnitude of the external forces acting on a fixed floating structure can be decreased compared with when there is no breakwater. In the existing literature that examines the interaction between floating structures or vertical walls and submerged breakwaters positioned in front of them, the floating structures are typically assumed to be fixed in place. In contrast, this study aims to analyze the interaction between a moving floating body and submerged breakwaters, with a focus on the resulting hydrodynamic performance. This approach is crucial for accurately assessing a WEC under realistic operational conditions, where the floating body experiences motion in multiple DoFs.

Numerous studies have been conducted to enhance the power generation performance of WECs. However, to the best of the authors' knowledge, the interaction between WECs and submerged breakwaters has not been extensively investigated. This study introduces a novel approach using Bragg resonance to enhance power generation by the WEC in the presence of two submerged breakwaters. The WEC was connected to a simple spring-type mooring system for station-keeping. Submerged breakwaters were strategically positioned in front of and behind the WEC to maximize the CWR of an HPA-type WEC and leveraging Bragg resonance, with the position and shape determined by an optimization analysis. The optimization analysis was performed by extending the optimization framework established in the authors' previous study [30]. A two-dimensional frequency domain boundary element method (FD-BEM) based on the linear potential flow theory was used for the hydrodynamic analysis, considering the interactions between the WEC and submerged breakwaters under irregular wave conditions. Advanced particle swarm optimization (PSO), one of the metaheuristic algorithms, was applied for the optimization analysis [31,32]. The design variables for the optimization analysis were set to the PTO damping coefficient, spring constant, and position and shape of the submerged breakwaters. Finally, the optimal values that maximized the CWR were analyzed.

2. Analysis Methods

In this study, the optimization analysis was performed by extending the framework linking the FD-BEM and the optimization program previously developed by the authors [30]. Figure 1 presents an overview of the calculation framework. The framework first received input data such as an objective (fitness) function and the boundaries of the design variables from the user. The optimization program executed the FD-BEM using the design variables of each particle and calculated the cost function using the output values of the FD-BEM. The design variables of each particle were updated so that the cost function converged to the maximum or minimum value as the generations (iteration number) passed on. The optimization process ended when the objective function satisfied the stopping criteria or reached the maximum number of iterations. The global best values determined the optimal values when the framework was terminated.
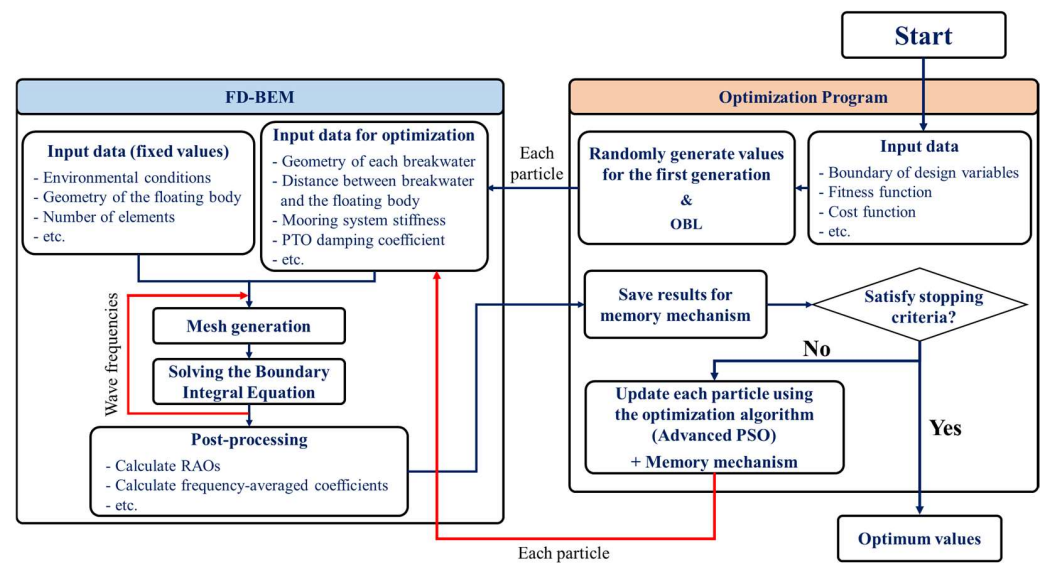
Figure 1. Overview of the framework linking the FD-BEM and the optimization program.

2.1. FD-BEM

The linear potential theory—which assumes the fluid in the computational domain is inviscid, irrotational, and incompressible—was used to solve the two-dimensional hydrodynamic problems. The fluid particle motion in the computational domain can be expressed using the velocity potential as follows [33]:

$$\Phi(x,z,t) = \text{Re}\left[\phi(x,z)e^{-i\omega t}\right] \tag{1}$$

where t, ϕ, ω, and Re are the time, complex velocity potential, wave frequency, and the real part of the complex value, respectively. The governing equation in the computational domain can be expressed using the Laplace equation as follows:

$$\nabla^2 \phi = 0 \tag{2}$$

$$\phi = \phi_I + \phi_D - i\omega \sum_{j=1}^{3} \xi_j \phi_{R,j} \tag{3}$$

where ϕ_I and ϕ_D are the incident wave potential and the diffraction potential, respectively. $\phi_{R,j}$ is the radiation potential due to the j-th mode of motion ($j = 1$ for surge, $j = 2$ for heave, and $j = 3$ for pitch). ξ_j is the magnitude of the j-th mode. The incident wave potential can be expressed as follows:

$$\phi_I = -i\frac{gH}{2\omega}\frac{\cosh k(z+h)}{\cosh kh}e^{ikx} \tag{4}$$

where g, H, k, h, x, and z are the gravitational acceleration, wave height, wavenumber, water depth, horizontal coordinate, and vertical displacement from the water surface, respectively.

The boundary integral equation can be derived from Green's second identity using Green's function, which is the fundamental solution of the Laplace equation.

$$\frac{1}{2}\phi + \int_{\Gamma}\left(\phi\frac{\partial G}{\partial \mathbf{n}}\right)d\Gamma = \int_{\Gamma}\left(G\frac{\partial \phi}{\partial \mathbf{n}}\right)d\Gamma \tag{5}$$

where $G = 1/(2\pi)\cdot\ln(1/r)$ is the two-dimensional Green's function and r, Γ, and $\mathbf{n}$ are the distance between the source and field points, the boundary of the computational domain, and outward normal vector at the boundary elements, respectively.

Figure 2 shows the WEC and two submerged breakwaters. The direction of the incident wave is the x-axis. The WEC had a rectangular cross-section. The origin of the

coordinate system was the center of gravity of the WEC, and it was assumed that the WEC was symmetrical with respect to the water surface. The WEC was connected to a PTO system and two mooring lines. The mooring lines were assumed to be simple spring elements with zero pre-tension. Each spring had the same spring constant, and the fairlead points and anchor points were symmetrical about the z-axis. The submerged breakwaters were also symmetrical in position about the z-axis and had the same geometry.
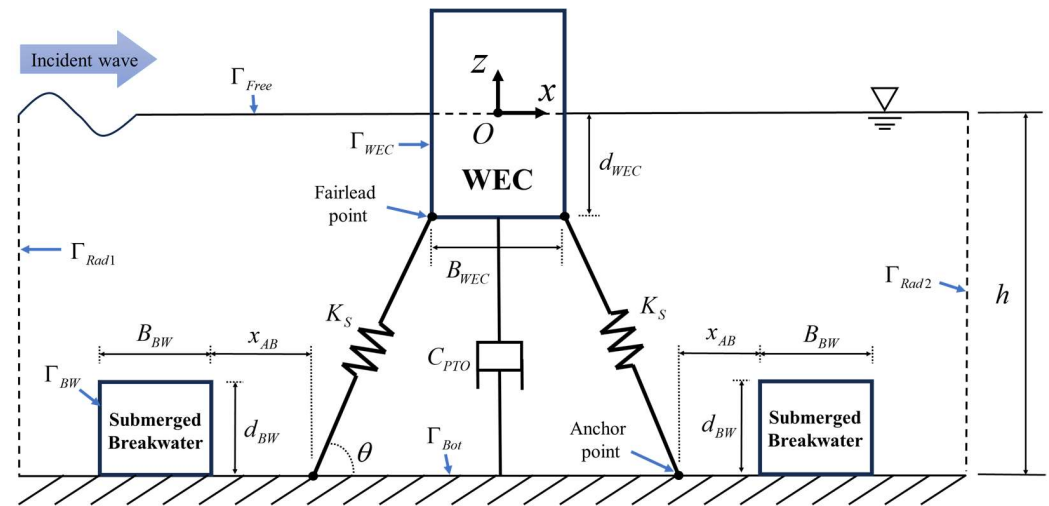

Figure 2. Description of the WEC and two submerged breakwaters.

The equation of motion of the WEC can be expressed as follows [34]:

$$\left[-\omega^2(\mathbf{M} + \mathbf{M}_a) - i\omega(\mathbf{C} + \mathbf{C}_{PTO}) + (\mathbf{K} + \mathbf{K}_M)\right]\zeta = \mathbf{F} \tag{6}$$

where $\mathbf{M}$ and $\mathbf{M}_a$ are the structural mass and added mass matrices, respectively. $\mathbf{C}$ and $\mathbf{C}_{PTO}$ are the radiation damping and PTO damping matrices, respectively. $\mathbf{K}$ and $\mathbf{K}_M$ are the structural stiffness and mooring stiffness matrices, respectively. ζ is the motion vector and $\mathbf{F}$ is the external force vector from the unit wave amplitude. The response amplitude operators (RAOs) could be calculated by dividing the external force vector by the left-hand side of Equation (6).

The structural mass and stiffness matrices can be expressed as follows [35]:

$$\mathbf{M} = \begin{bmatrix} m & 0 & mz_g \\ 0 & m & -mx_g \\ mz_g & -mx_g & I \end{bmatrix} \tag{7}$$

$$\mathbf{K} = \begin{bmatrix} 0 & 0 & 0 \\ 0 & \rho g B_{WEC} & 0 \\ 0 & 0 & \rho g \int_{\Gamma_{WEC}} x^2 n_z d\Gamma + \rho g V z_b - mgz_g \end{bmatrix} \tag{8}$$

where m and I are the mass and moment of inertia of the WEC, respectively. (x_g, z_g) are the coordinates of the center of gravity. B_{WEC} and V are the width and submerged volume of the WEC, respectively. n_z is the z-axis component of the normal vector and z_b is the center of buoyancy.

The elements of the added mass and radiation damping matrices in the i-th mode by the j-th motion could be calculated using the following equations:

$$M_{a,ij} = \rho \int_{\Gamma_{WEC}} \mathrm{Re}(\phi_{R,ij}) \, \mathbf{n} \, d\Gamma \tag{9}$$

$$C_{ij} = \rho\omega \int_{\Gamma_{WEC}} \text{Im}(\phi_{R,ij})\, \mathbf{n}\, d\Gamma \tag{10}$$

where ρ is the density of the fluid and Im is the imaginary part of the complex value.

The external forces acting on the WEC could be determined by integrating the hydrodynamic pressure acting on the submerged body surface. The external force vector could be calculated using the Bernoulli equation.

$$\mathbf{F} = i\rho\omega \left[\int_{\Gamma_{WEC}} (\phi_I + \phi_D)n_x\, d\Gamma \quad \int_{\Gamma_{WEC}} (\phi_I + \phi_D)n_z\, d\Gamma \quad \int_{\Gamma_{WEC}} (\phi_I + \phi_D)(r_{xg}n_z - r_{zg}n_x)\, d\Gamma \right]^T \tag{11}$$

where (r_{xg}, r_{zg}) are the displacement from the center of gravity to the body element.

In a frequency domain analysis, the force due to the PTO system must be linearized to validate the superposition principle [36]. The linearized PTO reaction force consists of two terms. The first term represents the damper, which is proportional to the velocity, and the second term represents the spring, which is proportional to the displacement. In this study, the spring term was not considered. Furthermore, the PTO force was calculated considering only the z-axis velocity, assuming that the x-axis velocity had little effect on the PTO force compared with the z-axis velocity.

$$F_{PTO} = -C_{PTO}\dot{z} = i\omega C_{PTO}z \tag{12}$$

where C_{PTO} is the PTO damping coefficient. The time-averaged power produced by the PTO system and the power contained in the incident wave of the unit crest length could be calculated as follows [37]:

$$P_{WEC,reg}(\omega) = \frac{1}{2}C_{PTO}\,\omega^2|RAO|^2A^2 \tag{13}$$

$$P_{I,reg}(\omega) = \frac{1}{4}\frac{\rho g \omega}{k}\left(1 + \frac{2kh}{\sinh 2kh}\right)A^2 \tag{14}$$

where A is the wave amplitude. The optimal C_{PTO} to maximize P_{WEC}, depending on the wave frequency, could be obtained by substituting the heave RAO into Equation (13) and then differentiating it [38].

$$C_{PTO,opt}(\omega) = \sqrt{C(\omega)^2 + [(K_{22} + K_{M,22})/\omega - \omega\{M_{22} + M_{a,22}(\omega)\}]^2} \tag{15}$$

On the other hand, this study assumed that C_{PTO} had a constant value in each simulation because actual ocean waves are irregular. The capture width ratio (CWR) could be calculated as follows:

$$CWR = \frac{P_{WEC}}{B_{WEC}P_I} \tag{16}$$

The mooring system was considered for the station-keeping of the WEC. The mooring stiffness matrix using a simple spring element could be obtained using the following equation:

$$\mathbf{K}_M = K_S \begin{bmatrix} \cos^2\theta & \cos\theta\sin\theta & x_{fg}\cos\theta\sin\theta - z_{fg}\cos^2\theta \\ & \sin^2\theta & x_{fg}\sin^2\theta - z_{fg}\cos\theta\sin\theta \\ symm. & & (x_{fg}\sin\theta - z_{fg}\cos\theta)^2 \end{bmatrix} \tag{17}$$

where K_S is the spring constant, θ is the angle between the x-axis and the displacement vector from the anchor point to the fairlead point, and (x_{fg}, z_{fg}) is the displacement from the center of gravity to the fairlead point.

The diffraction and radiation potentials in Equations (9)–(11) could be obtained by solving the diffraction and radiation problems, respectively. These problems had the following boundary conditions and could be solved by substituting them into Equation (5) [39].

$$\begin{cases} \frac{\partial \phi_D}{\partial \mathbf{n}} - \frac{\omega^2}{g}\phi_D = 0 & on \; \Gamma_{Free} \\ \frac{\partial(\phi_D - \phi_I)}{\partial \mathbf{n}} - ik(\phi_D - \phi_I) = 0 & on \; \Gamma_{Rad1} \\ \frac{\partial \phi_D}{\partial \mathbf{n}} - ik\phi_D = 0 & on \; \Gamma_{Rad2} \\ \frac{\partial \phi_D}{\partial \mathbf{n}} = 0 & on \; \Gamma_{Bot} \; and \; \Gamma_{BW} \\ \frac{\partial \phi_D}{\partial \mathbf{n}} = -\frac{\partial \phi_I}{\partial \mathbf{n}} & on \; \Gamma_{WEC} \end{cases}, \quad \begin{cases} \frac{\partial \phi_{R,j}}{\partial \mathbf{n}} - \frac{\omega^2}{g}\phi_{R,j} = 0 & on \; \Gamma_{Free} \\ \frac{\partial \phi_{R,j}}{\partial \mathbf{n}} - ik\phi_{R,j} = 0 & on \; \Gamma_{Rad1} \; and \; \Gamma_{Rad2} \\ \frac{\partial \phi_{R,j}}{\partial \mathbf{n}} = 0 & on \; \Gamma_{Bot} \; and \; \Gamma_{BW} \\ \frac{\partial \phi_{R,j}}{\partial \mathbf{n}} = v_j \cdot n_j & on \; \Gamma_{WEC} \end{cases} \quad (18)$$

where v_j refers to the velocity of the j-th mode.

The reflection and transmission coefficients at the radiation boundaries could be calculated using the following velocity potentials [28]:

$$K_R(\omega) = \frac{i\omega}{gAN_0^2}\left[\int_{-h}^0 \phi|_{Rad,1}Z_0(z)dz\right] - 1 \quad (19)$$

$$K_T(\omega) = \frac{i\omega}{gAN_0^2}\left[\int_{-h}^0 \phi|_{Radi,1}Z_0(z)dz\right] \quad (20)$$

where K_R and K_T are the reflection and transmission coefficients, respectively. $Z_0(z) = \cosh k(z + h)/\cosh kh$ is the vertical eigenfunction, i.e., $N_0^2 = \int_{-h}^0 Z_0^2(z)dz$. According to the energy conservation principle, the total energy of the reflected and transmitted waves and P_{WEC}/P_I were constant ($K_R^2 + K_T^2 + (P_{WEC}/P_I) = 1$) [40].

The JONSWAP spectrum was applied as the wave spectrum, and it could be expressed as follows [41]:

$$\begin{aligned} S(\omega) &= \beta\frac{H_S^2\omega_P^4}{\omega^5}\exp\left[-\frac{5}{4}\left(\frac{\omega_P}{\omega}\right)^4\right]\gamma^\alpha \\ \alpha &= \exp\left[-\frac{(\omega - \omega_P)^2}{2\sigma^2\omega_P^2}\right] \\ \beta &= \frac{0.06238}{0.230 + 0.0336\gamma - 0.185(1.9 + \gamma)^{-1}}(1.094 - 0.01915\ln\gamma) \\ \sigma &= \begin{cases} 0.07 & when \; \omega < \omega_P \\ 0.09 & when \; \omega > \omega_P \end{cases} \end{aligned} \quad (21)$$

where H_S, ω_P, and γ are the significant wave height, peak wave frequency, and peak enhancement factor, respectively.

Under irregular wave conditions, P_{WEC} and the theoretical P_I could be calculated as follows [42]:

$$P_{WEC} = C_{PTO}\int_0^\infty \omega^2|RAO(\omega)|^2S(\omega)d\omega \quad (22)$$

$$P_I = \frac{\rho g^2 H_S^2 T_P}{64\pi} \quad (23)$$

where T_P is the peak period ($T_P = 2\pi/\omega_P$).

In addition, frequency-averaged reflection and transmission coefficients could be obtained using the following equations [43]:

$$\overline{K}_R = \sqrt{m_{0,R}/m_{0,S}} \quad (24)$$

$$\overline{K}_T = \sqrt{m_{0,T}/m_{0,S}} \quad (25)$$

where $m_{0,R}$ and $m_{0,T}$ are zeroth moments of the reflected ($S_R(\omega) = |K_R(\omega)|^2S(\omega)$) and transmitted spectra ($S_T(\omega) = |K_T(\omega)|^2S(\omega)$), respectively. $m_{0,S}$ is the zeroth moment of the wave spectrum.

2.2. Metaheuristic Algorithm

Metaheuristic algorithms can be applied to obtain the maximum or minimum cost functions based on the objective function in an optimization analysis with multiple design variables. Particle swarm optimization (PSO) is a swarm-based algorithm inspired by the social behaviors observed in bird flocking and fish schooling [44,45]. It is esteemed for its simplicity in both implementation and coding, requiring only a few parameters such as the inertia weight, cognitive ratio, and social ratio. These parameters play a crucial role in influencing the performance of the optimization process. The versatility of PSO allows for its hybridization with other algorithms, thereby expanding its applicability and enhancing its performance across a diverse range of optimization scenarios [45]. This study used advanced PSO, which improves the shortcomings of general PSO, for the optimization analysis [31,44,46]. Jeong and Koo [32] showed the superiority of advanced PSO by performing a comparative analysis of various metaheuristic algorithms.

General PSO consists of Np particles for each generation (iteration). Each particle has Nd design variables and the solution obtained from those design variables becomes the value of the particle. Each design variable of a particle is called a position and the position is updated based on the velocity calculated using the best value (personal best value) and the global best value of each particle. The velocity of the k-th design variable of the j-th particle of the i-th generation can be expressed as follows [31]:

$$V_{i,j}^k = \alpha \, V_{i-1,j}^k + c_1 \, rand_1 \left(Pbest \left(X_{i-1,j}^k \right) - X_{i-1,j}^k \right) + c_2 \, rand_2 \left(Gbest \left(X_{i-1}^k \right) - X_{i-1,j}^k \right) \quad (26)$$

where $rand$ denotes a random number between 0 and 1. $V_{i,j}^k$ and $X_{i-1,j}^k$ are the velocity and position of each design variable, respectively. $Pbest(\mathbf{X}_{i-1,j})$ denotes the position vector where the cost function of the j-th particle has the best value until the previous generation and $Gbest(\mathbf{X}_{i-1})$ denotes the best position vector of the particle with the best cost function among all particles up to the previous generation. α is the linear decreasing inertia weight and can be calculated as follows:

$$\alpha = \alpha_{\max} - \frac{Iter_i}{Iter_{\max}} (\alpha_{\max} - \alpha_{\min}) \quad (27)$$

where $Iter_i$ and $Iter_{\max}$ are the i-th generation and the maximum number of generations, respectively. $\alpha_{\max}$ and $\alpha_{\min}$ are the initial and final values of α, respectively. PSO shows excellent performance when α starts from a value close to 1 and decreases linearly to 0.4 [46]. Accordingly, an $\alpha_{\max}$ of 0.8 and an $\alpha_{\min}$ of 0.4 were applied. c_1 and c_2 were described by the sine cosine acceleration coefficients (SCACs) [31] as follows:

$$c_1 = \partial \sin \left(\frac{\pi}{2} \left(1 - \frac{Iter_j}{Iter_{\max}} \right) \right) + \delta \quad (28)$$

$$c_2 = \partial \cos \left(\frac{\pi}{2} \left(1 - \frac{Iter_j}{Iter_{\max}} \right) \right) + \delta \quad (29)$$

where ∂ and δ were applied as 2 and 0.5, respectively [31].

After calculating the velocity of each design variable using Equation (26), the position of the next generation could be updated as follows:

$$X_{i,j}^k = X_{i-1,j}^k + V_{i,j}^k \quad (30)$$

The opposition-based learning technique was applied to obtain the initial design variables of each particle of the first generation [47]. A memory mechanism was applied to omit the positions calculated in previous simulations [48].

3. Numerical Results

3.1. Validation of the FD-BEM

The two-dimensional frequency domain numerical analysis method (FD-BEM) used to consider the interaction between a fixed surface-piercing body and a submerged breakwater was validated in the authors' previous research [30]. In this study, this validated framework was extended to optimize the power generation of an HPA-WEC integrated with submerged breakwaters. A module to solve radiation problems was incorporated into the FD-BEM developed in previous research to analyze the floating body motion. The validity of the FD-BEM for floating body motion was validated by comparing the heave-added mass and radiation damping results for a rectangular-shaped floating body with the theoretical results.

Figure 3 compares the hydrodynamic coefficients for a rectangular-shaped floating body at different ratios of width (B) to draft (d) [49]. In the high-frequency range, slight differences in the added mass of the floating body were observed, which were believed to be due to issues such as mesh problems at very small wavelengths. In most frequency ranges (for $\omega\sqrt{B/2g}$ values below 1.5), the overall trends and magnitudes were well aligned.
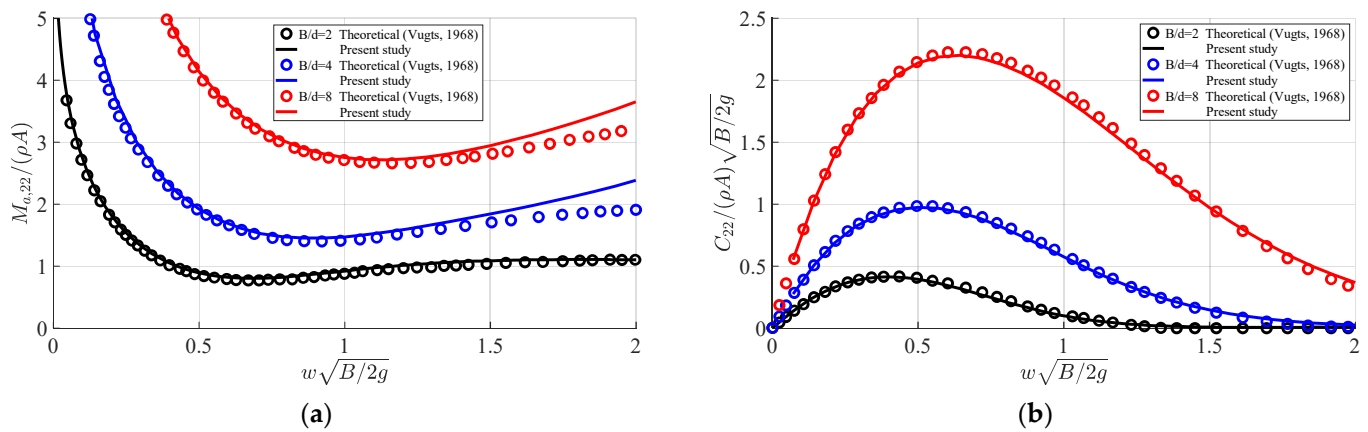

Figure 3. Comparison of the heave-added mass and radiation damping of a rectangular-shaped floating body: (**a**) heave-added mass; (**b**) heave radiation damping. Vugts, 1968 [49].

Direct validations with other studies on the multi DoF motions of WECs with submerged breakwaters remain limited. Nonetheless, the interaction problem between fixed floating bodies and submerged breakwaters has been previously verified. The robustness of the present method was further established through an additional validation using the radiation problem conducted in this study. This ensures the method's generality and applicability to HPA-WEC systems, underscoring the improvements and unique aspects of our approach.

3.2. Irregular Wave Conditions

Gangneung, on the coast of Korea, was selected for the real sea conditions, as shown in Figure 4a. The one-year average wave data (14 November 2022 to 13 November 2023) were obtained from the Wave Information Network of Korea [50,51]. Over the course of one year, 16,103 wave data were collected at 30 min intervals, with an overall availability of 91.9% of the total 17,520 data. It was assumed that all waves acted consistently in the same direction. The average significant wave height and peak period were calculated using the average values of these wave data, and were 0.84 m and 6.33 s (0.99 rad/s), respectively.

The JONSWAP spectrum was applied to generate a wave spectrum [41]. Figure 4b shows the JONSWAP spectrum with an enhancement factor (γ) of 3.3 when the corresponding environmental conditions were applied. The water depth was 34 m and the applied seawater density was 1025 kg/m^3. The direction of all incident waves was the same to estimate the potential maximum power production. The wave frequencies for the irregular

wave analysis ranged from 0.83 rad/s to 1.13 rad/s, which represented a range of incident wave power over 30% of the wave power of the peak frequency. The interval of the wave frequency was 0.02 rad/s; a total of 16 regular waves were considered. The wave amplitude for the regular wave analysis was calculated using the following equation [52]:

$$A = \sqrt{2S(\omega)\Delta\omega} \qquad (31)$$

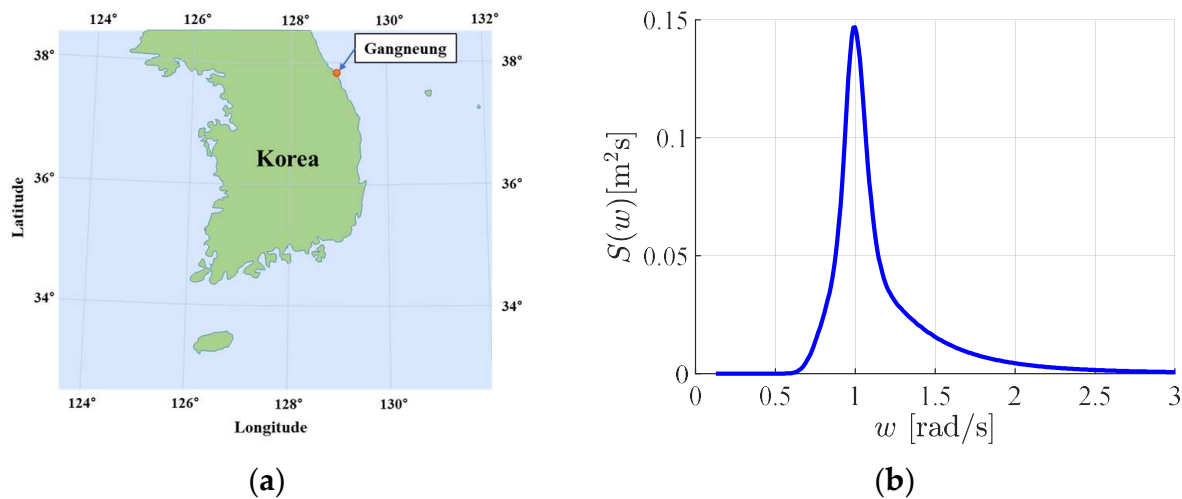where A is the wave amplitude and $\Delta\omega$ is the interval of the wave frequency.

(a)

(b)

Figure 4. Wave buoy location and the corresponding JONSWAP wave spectrum: (**a**) Gangneung, on the Korean coast; (**b**) wave spectrum ($H_S = 0.84$ m, $T_P = 6.33$ s, and $\gamma = 3.3$) [51].

3.3. Optimization Analysis

Figure 5 shows the four cases used for the optimization analysis. In Case 1, there was no breakwater and it became the standard to compare the results depending on the presence of the submerged breakwater. Cases 2 and 3 analyzed the situations where a single breakwater was close to the incident wave direction (front) and far from the incident wave direction (rear), respectively, based on the WEC. Case 4 was the same as shown in Figure 2, with two breakwaters symmetrically positioned to the *z*-axis based on the WEC.

In all cases, the structural properties of the WEC were the same, as listed in Table 1. The width of the WEC (B_{WEC}) was determined to be 0.15 h (5.1 m) according to the diameter of the WEC, which was in the range of 5% to 10% of the prevailing wavelength [53]. The draft of the WEC (d_{WEC}) was set to 0.3 h (10.2 m). A sufficiently wide resonance bandwidth should be considered to determine the draft of a WEC [17]. The draft of the WEC was assumed to be sufficient because this study applied the JONSWAP spectrum, which had a relatively small resonance bandwidth.

The fairlead points, to which a simple spring-type mooring system was connected to the WEC, were at both ends of the underside of the WEC. The anchor point was located on the sea bottom, relatively close to the WEC and one B_{WEC} away from the fairlead point, so the breakwaters were close to the WEC. The center of gravity of the WEC was set at the water surface, so the pitch stability was expected to be unstable. Lowering the center of gravity and raising the fairlead point above the center of gravity increased the pitch stability.
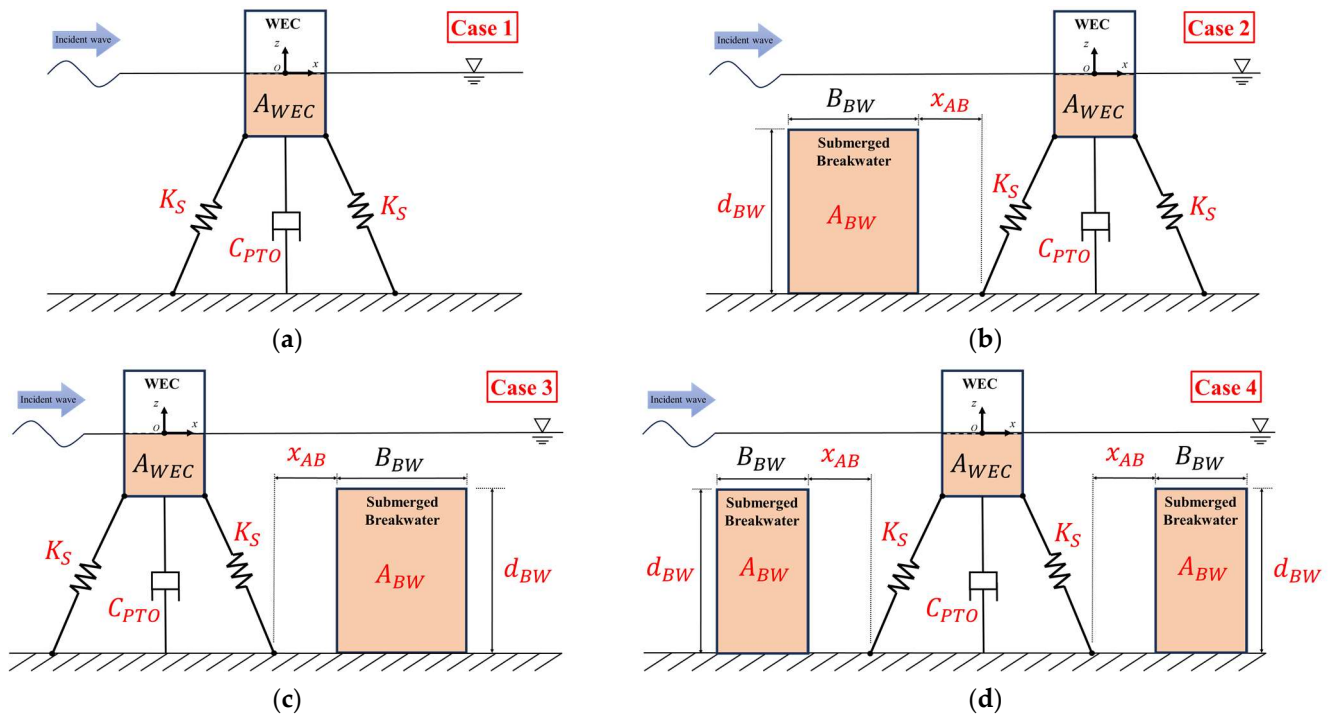
Figure 5. Description of the four cases for the optimization analysis: (**a**) Case 1 (no breakwater); (**b**) Case 2 (single breakwater—front); (**c**) Case 3 (single breakwater—rear); (**d**) Case 4 (two breakwaters).

Table 1. Structural properties of the floating body.

Description	Value
Width (B_{WEC})	5.1 m
Draft (d_{WEC})	10.2 m
Overall length	20.4 m
Submerged area (A_{WEC})	52.02 m^2
Center of gravity	(0, 0)
Mass	53,320.5 kg
Moment of inertia	1,964,727 kg·m^2
Heave stiffness (K_{22})	51,260.9 N/m
Fairlead points	(± 2.55, -10.2) m
Anchor points	(± 7.65, -34) m

Table 2 lists the boundaries of the design variables for the four cases. The PTO damping coefficient (K_S) and spring constant (C_{PTO}) were applied as design variables for the optimization analysis. K_S affects the natural frequency and stability of a floating body. C_{PTO} not only affects the power production (heave RAO of the WEC), but also plays a role in reducing the snap load and load fluctuation acting on the mooring lines [54]. This role of C_{PTO} can influence the stability of mooring systems when used as constraints in an optimization analysis. In addition, the distance between the breakwater and the anchor point (x_{AB}), the area of the breakwater ($A_{BW} = A_{Ratio}A_{WEC}$), and the height of the breakwater (d_{BW}) were set as additional design variables. A_{BW} was related to the installation cost of the breakwater and was set as A_{Ratio}, which was the ratio of the breakwater to the submerged area of the WEC.

Case 1 had two design variables and Cases 2 to 4 had five. The total number of possible simulations was 45,000 (300×150) for Case 1 and approximately 65 billion ($300 \times 150 \times 201 \times 141 \times 51$) for the others. Considering the total number of simulations, the number of particles was set to 100 for Case 1 and 500 for the other cases. The maximum number of generations (iterations) was set to 500, which was the same in all cases. The objective function for the optimization analysis was set to maximize the CWR under irregular wave

conditions, as shown in Equations (16), (22) and (23). Table 3 lists the PC configuration and the software tool used for the optimization analysis. All analyses were performed using the same PC and the time required for one simulation was six seconds or less.

Table 2. Boundaries of the design variables for optimization analysis.

Design Variables	Lower Limit	Upper Limit	Step Size
C_{PTO} [Ns/m]	100	30,000	100
K_S [N/m]	100	15,000	100
x_{AB}/B_{WEC}	0.0	20.0	0.1
$A_{Ratio}(= A_{BW}/A_{WEC})$	1.0	15.0	0.1
d_{BW}/h	0.3	0.8	0.01

Table 3. PC configuration and software tool for simulation (Intel, Santa Clara, CA, USA).

Components	Description
CPU	Intel (R) Xeon (R) Platinum 8260 (2.40 GHz)
Cores of CPU	48
RAM	192 GB
OS	Windows 10
Compiler	Intel® Fortran Compiler Classic 2021.8.0 [Intel(R) 64]

Table 4 lists the total simulation time and number of simulations required for the optimization analysis. Case 1 had two design variables and 100 particles, so all particles converged to the same design variables within a relatively short simulation time. Cases 2 to 4 used 500 particles for 5 design variables, so the simulation took longer than 30 h. The total number of simulations in Case 2 was approximately 10,000 more than in Cases 3 and 4, possibly because the randomly generated first-generation design variables were far from the optimal values.

Table 4. Total simulation time and number of simulations.

Cases	Total Simulation Time [h]	Converged Iteration	Total Number of Simulations
Case 1	3.37	152	3354
Case 2	40.29	197	36,939
Case 3	30.46	213	26,504
Case 4	33.65	242	26,938

Table 5 lists the optimized design variables obtained from the optimization analysis and corresponding parameters. C_{PTO} and K_S exhibited the smallest values in Case 1 and the largest values in Case 4. This was because (referring to B_{BW}) the influence on the movement of the WEC increased as the area of the submerged breakwater increased. Therefore, the motion response of the WEC was influenced by the position and shape of the submerged breakwater.

Figure 6a shows the heave radiation damping (C_{22}) of the WEC. In the peak wave frequency range, the value of C_{22} in Case 4 was more than twice that of the other cases. Furthermore, in all cases, the optimized C_{PTO} had a larger value than the optimal PTO damping coefficient value at the peak wave frequency ($C_{PTO,opt}(\omega_P)$) obtained using Equation (15). Hence, Equation (15) provided the optimal value for regular waves. Under irregular wave conditions, C_{PTO} must be obtained from an optimization analysis to maximize the CWR.

Figure 6b shows the heave RAO of the WEC. Resonance of the heave RAO occurred within the peak wave frequency range for all cases. In addition, C_{PTO} and K_S converged so that the heave resonance frequency of the WEC and the peak wave frequency became closer. In the peak frequency range, the heave RAO of Case 4 was the smallest, while the

other three cases had similar values. The CWR was proportional to the product of the square of the RAO and C_{PTO}, as shown in Equation (22). Case 4 had the smallest RAO, but C_{PTO} had a larger value than the other cases, so the produced wave power had the largest value. In Cases 3 and 4, the resonance of the heave RAO occurred near low frequencies, which was attributed to the WEC having a low-frequency mode due to reflected waves from the rear breakwater.

In the presence of the breakwater (Cases 2 to 4), A_{Ratio} was the smallest in Case 2, indicating that its width became relatively thin compared to its height, necessitating an additional analysis for stability against overturning moments. Cases 3 and 4 converged to results where the area of the breakwater exceeded 10 times the area of the WEC. As the installation cost of the breakwater was proportional to its area, adjusting the range of the breakwater height was required to reduce the installation costs. The optimal values for d_{BW} all converged to the upper boundary, suggesting that the influence of the breakwater on water particles became more significant as it approached the water surface [30].

Table 5. Optimal values and corresponding parameters of the submerged breakwaters.

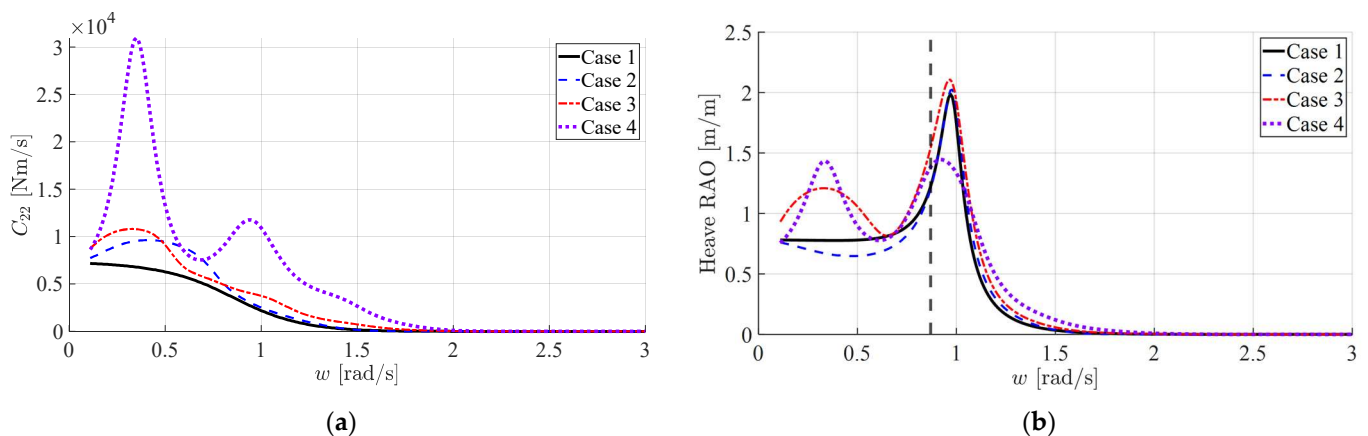| Parameters		Case 1	Case 2	Case 3	Case 4
Optimized design variables	C_{PTO} [Ns/m]	5700	6200	7600	13,700
	K_S [N/m]	7500	7700	8800	12,400
	x_{ab}/B_{WEC}	-	1.7	0.0	0.0
	$A_{Ratio}(=A_{BW}/A_{WEC})$	-	2.5	11.6	12.3
	d_{BW}/h	-	0.8	0.8	0.8
Corresponding parameters	$B_{BW}(=A_{BW}/d_{BW})$ [m]	-	4.78	22.19	20.85
	$C_{PTO,opt}(\omega_P)$ [Ns/m]	2825	2796	4241	11,178

Figure 6. Heave radiation damping and heave RAO of the WEC: (**a**) heave radiation damping; (**b**) heave RAO (vertical dash line: natural frequency of a freely floating body at 0.87 rad/s).

The optimal values presented in Table 5 resulted from an irregular wave analysis considering a wave frequency range of 0.83 rad/s to 1.13 rad/s. However, analyzing only within this range may not have fully accounted for all environmental wave conditions. Therefore, a numerical analysis covering a broader wave frequency range was conducted by performing an irregular wave analysis at 0.01 rad/s intervals from 0.1 rad/s to 3.0 rad/s using the optimal values from Table 5 for comparison.

Table 6 lists the CWR and frequency-averaged reflection ($\overline{K}_R$) and transmission ($\overline{K}_T$) coefficients calculated using the optimal values. The numbers inside parentheses represent the ratios relative to Case 1. In Case 4, the CWR was approximately twice as large as in Case 1 and approximately 66% greater than in Case 2. On the other hand, it was approximately 11% larger than Case 3 and the difference was relatively small compared with the other cases. This was attributed to the significant influence of the reflected waves

generated from the breakwater when installed behind the WEC (rear). In contrast, the impact of the breakwater on the WEC were relatively small if it was installed in front of the WEC. $\overline{K}_R$ changed by less than 5% compared with Case 1 because of the presence of the breakwater, but $\overline{K}_T$ decreased by approximately 7% and 13% in Cases 3 and 4, respectively. Case 4 reduced the frequency-averaged transmitted wave energy by approximately 25% compared with Case 1 because the wave energy was proportional to the square of the wave height. The above results confirmed that Case 4 yielded the highest power production and coastal safety. On the other hand, the installation cost was at least twice that of Cases 2 and 3 because two submerged breakwaters needed to be installed.

Table 6. CWR, frequency-averaged reflection, and transmission coefficients ($0.1 \leq \omega \leq 3.0$ rad/s) (the numbers inside parentheses represent ratios relative to Case 1).

Cases	CWR	$\overline{K}_R$	$\overline{K}_T$
Case 1	2.95×10^{-2} (1.00)	0.484 (1.000)	0.791 (1.000)
Case 2	3.54×10^{-2} (1.20)	0.487 (1.006)	0.772 (0.975)
Case 3	5.30×10^{-2} (1.80)	0.461 (0.953)	0.734 (0.928)
Case 4	5.88×10^{-2} (1.99)	0.499 (1.030)	0.687 (0.868)

Figure 7 shows the power produced by the WEC under irregular wave conditions according to ω, as shown in Equation (32).

$$dP_{WEC}(\omega) = C_{PTO}\,\omega^2 |RAO(\omega)|^2\, S(\omega)\, d\omega \tag{32}$$

The power production at the peak wave frequency was the largest in Case 3, but the CWR in the entire range had the largest value in Case 4 because the resonance bandwidth was the widest in Case 4. Case 1 had the smallest CWR because there was no means to amplify the CWR except for C_{PTO} and K_S. Taking the CWR of Case 4 in Table 6 as an example, the CWR at 0.83 to 1.13 rad/s (5.43×10^{-2}) was calculated to be approximately 92.4% of the CWR over the entire range. Therefore, when a large number of simulations are required (such as for an optimization analysis), sufficiently valid results may be provided even if the analysis is performed considering only the resonance bandwidth to reduce the total simulation time.
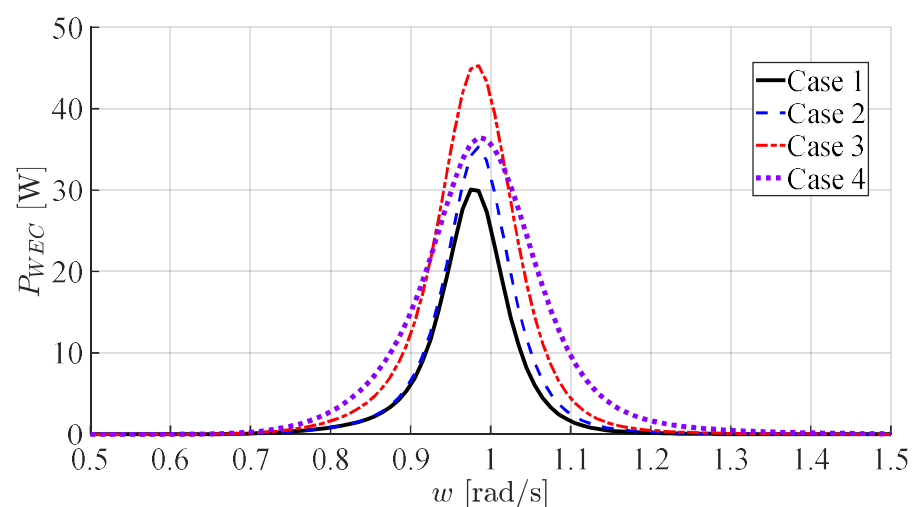

Figure 7. Power produced under irregular wave conditions.

Figure 8a shows the geometric optimal values for Case 4. The distance between the ends of the breakwaters (x_{BB}) converged to 62.42 m, which aligned with the wavelength at the peak wave frequency. Figure 8b presents a scatter plot of the simulation results obtained from the optimization analysis of Case 4 in terms of x_{BB}. The CWR converged to its maximum value as x_{BB} approached the wavelength of the peak wave frequency (λ_P). This was believed to occur because the surface wave met a type of Bragg condition because of the WEC and the two submerged breakwaters, resulting in a substantial amplification of Bragg-scattered waves. Generally, the condition for Bragg resonance is when the distance between the centers of periodic bodies (or bottom ripples) is proportional to half the wavelength [55].

$$x_{Bragg} = n\lambda/2 \quad \text{for } n = 1, 2, \cdots \tag{33}$$

On the other hand, the Bragg condition changed so that x_{BB} matched λ_P because of the changes in the flow field caused by the presence of the WEC. This could be indirectly confirmed using Figure 8b, where the CWR rapidly decreased when $x_{BB}/\lambda_P > 1$. The CWR increased when $x_{BB}/2$ approached the anchor point. However, it would be impossible to install in practice because in this situation, B_{BW} was extremely thin.

From the above results, it was elucidated that maximizing power production in an HPA-WEC design requires the PTO damping coefficient and spring constant to be determined to approach the heave resonance frequency of the WEC within the peak wave frequency range. Furthermore, a method was proposed to induce a type of Bragg resonance by installing submerged breakwaters in front of and behind the WEC, with the distance between their ends matching the wavelength of the peak wave frequency. On the other hand, for a realistic design, factors such as installation costs and stability criteria like the overturning moment and buoyancy should also be considered during the design phase.
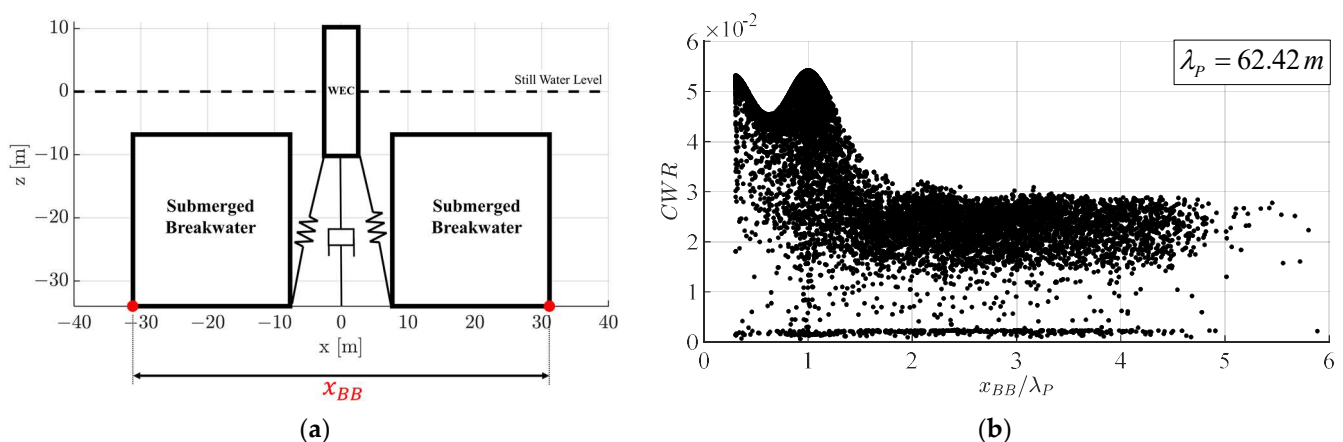

Figure 8. Illustration of the distance between the ends of breakwaters and scatter plot of the CWR: (**a**) illustration of x_{BB}; (**b**) scatter plot of the CWR.

4. Conclusions

Numerous studies have been conducted to enhance the power generation performance of WECs. However, to the best of the authors' knowledge, the interaction between WECs and submerged breakwaters has not been extensively investigated. In this study, we performed an optimization analysis to maximize the power generation of an HPA-WEC by installing submerged breakwaters both in front of and behind a WEC. This approach could significantly improve the performance of WEC systems and enhance coastal stability. These findings contribute to the scientific understanding of optimizing submerged breakwaters for HPA-WEC applications.

The design variables were the PTO damping coefficient (C_{PTO}), spring constant (K_S), submerged breakwater position, and shape. The optimization results demonstrated that varying C_{PTO} and K_S along with adjusting the position and shape of submerged breakwa-

ters significantly influenced the WEC's motion response and the power produced. C_{PTO} and K_S exhibited the smallest values in the case of no breakwater (Case 1 in the text) and the largest values in the case with two breakwaters (Case 4 in the text). In all cases, the optimized C_{PTO} had a larger value than the optimal PTO damping coefficient value at the peak wave frequency ($C_{PTO,opt}(\omega_P)$). This underscores the necessity of determining C_{PTO} using an optimization analysis under irregular wave conditions. Furthermore, C_{PTO} and K_S converged so that the heave resonance frequency of the WEC and the peak wave frequency became closer. This convergence highlighted that in HPA-WEC designs, maximizing power production requires the determination of C_{PTO} and K_S to approach the heave resonance frequency of the WEC within the peak wave frequency range.

The optimization results also revealed that the CWR increased nearly twice for two breakwaters (Case 4 in the text) compared with the case without a breakwater (Case 1 in the text). On the other hand, even when there was a breakwater behind the WEC (Case 3 in the text), the CWR increased by approximately 80%. A WEC should be designed considering the importance of the CWR and submerged breakwater installation costs. In terms of coastal stability, Case 4 was the best and the magnitude of the transmitted wave was reduced by approximately 13% (the energy of the transmitted wave was reduced by approximately 25%).

In addition, the CWR converged to the largest value when the distance between the breakwater endpoints equaled the wavelength of the peak wave frequency. This was attributed to a type of Bragg resonance where the surface wave acting on the WEC was amplified. In the basic design stage for HPA-WECs, power generation and coastal stability could be increased by considering two breakwaters.

The findings of this study provide valuable insights into the design and optimization of an HPA-WEC. It was confirmed that tuning the PTO damping coefficient and spring constant to align the heave resonance frequency of the WEC with the peak wave frequency range is crucial to maximize power production. Furthermore, the study demonstrated that the implementation of two submerged breakwaters could significantly enhance the CWR through the induction of Bragg resonance, with the optimal configuration being the distance between the breakwater endpoints matching the wavelength of the peak wave frequency. These results suggest that incorporating two breakwaters during the initial design phase of HPA-WECs could improve both power generation and coastal stability. In practical design applications, installation costs and stability criteria should be thoroughly evaluated and the optimization analysis methods presented in this study should be effectively utilized to inform the design process.

The limitations of this study and future recommendations can be summarized as follows:

- Design variables: The study exclusively utilized rectangular shapes for the WEC and submerged breakwaters. Future optimization analyses should consider a variety of shapes to identify more efficient structural configurations.
- Nonlinearity: This study was conducted in a frequency domain based on the linear potential flow theory. Future research should include nonlinear analyses in the time domain to account for nonlinear boundary conditions and external forces.
- Stability of the breakwater: Stability criteria, including considerations of self-weight, buoyancy, and overturning moments acting on the submerged breakwater, should be integrated as constraints in the optimization analysis.
- Applications: This study focused solely on the power production of a WEC. For practical applications, an analysis of the levelized cost of energy (LCOE) should be conducted, taking into account the manufacturing, installation, operation, and maintenance costs of the WEC.

References

1. Jacobson, M.Z.; Delucchi, M.A.; Bauer, Z.A.F.; Goodman, S.C.; Chapman, W.E.; Cameron, M.A.; Bozonnat, C.; Chobadi, L.; Clonts, H.A.; Enevoldsen, P.; et al. 100% Clean and Renewable Wind, Water, and Sunlight All-Sector Energy Roadmaps for 139 Countries of the World. *Joule* **2017**, *1*, 108–121. [CrossRef]
2. Clément, A.; McCullen, P.; Falcão, A.; Fiorentino, A.; Gardner, F.; Hammarlund, K.; Lemonis, G.; Lewis, T.; Nielsen, K.; Petroncini, S.; et al. Wave energy in Europe: Current status and perspectives. *Renew. Sustain. Energy Rev.* **2002**, *6*, 405–431. [CrossRef]
3. Ahamed, R.; McKee, K.; Howard, I. Advancements of Wave Energy Converters Based on Power Take Off (PTO) Systems: A Review. *Ocean Eng.* **2020**, *204*, 107248. [CrossRef]
4. Gaspar, J.F.; Calvário, M.; Kamarlouei, M.; Soares, C.G. Power Take-off Concept for Wave Energy Converters Based on Oil-hydraulic Transformer Units. *Renew. Energy* **2016**, *86*, 1232–1246. [CrossRef]
5. Falcão, A. Wave energy utilization: A review of the technologies. *Renew. Sustain. Energy Rev.* **2010**, *14*, 899–918. [CrossRef]
6. IRENA. *Innovation Outlook: Ocean Energy Technologies*; International Renewable Energy Agency: Abu Dhabi, United Arab Emirates, 2020.
7. Guo, B.; Ringwood, J.V. Geometric Optimisation of Wave Energy Conversion Devices: A Survey. *Appl. Energy* **2021**, *297*, 117100. [CrossRef]
8. Guo, B.; Wang, T.; Jin, S.; Duan, S.; Yang, K.; Zhao, Y. A Review of Point Absorber Wave Energy Converters. *J. Mar. Sci. Eng.* **2022**, *10*, 1534. [CrossRef]
9. Ringwood, J.V.; Bacelli, G.; Fusco, F. Energy-maximizing Control of Wave-energy Converters: The Development of Control System Technology to Optimize Their Operation. *IEEE Control Syst. Mag.* **2014**, *34*, 30–55.
10. Mustapa, M.A.; Yaakob, O.B.; Ahmed, Y.M.; Rheem, C.K.; Koh, K.K.; Adnan, F.A. Wave Energy Device and Breakwater Integration: A Review. *Renew. Sustain. Energy Rev.* **2017**, *77*, 43–58. [CrossRef]
11. Kim, T.; Lee, W.D.; Kwon, Y.; Kim, J.; Kang, B.; Kwon, S. Prediction of Wave Transmission Characteristics of Low Crested Structures Using Artificial Neural Network. *J. Ocean Eng. Technol.* **2022**, *36*, 313–325. [CrossRef]
12. Hwang, Y.; Do, K.; Kim, I.; Chang, S. Field observation and Quasi-3D numerical modeling of coastal hydrodynamic response to submerged structures. *J. Ocean Eng. Technol.* **2023**, *37*, 68–79. [CrossRef]
13. Falnes, J. A Review of Wave-energy Extraction. *Mar. Struct.* **2007**, *20*, 185–201. [CrossRef]
14. Zhang, H.; Zhou, B.; Vogel, C.; Willden, R.; Zang, J.; Zhang, L. Hydrodynamic Performance of a Floating Breakwater as an Oscillating-buoy Type Wave Energy Converter. *Appl. Energy* **2020**, *257*, 113996. [CrossRef]
15. Ning, D.; Zhao, X.; Göteman, M.; Kang, H. Hydrodynamic Performance of a Pile-Restrained WEC-Type Floating Breakwater: An Experimental Study. *Renew. Energy* **2016**, *95*, 531–541. [CrossRef]
16. Zhao, X.; Ning, D.; Zhang, C.; Kang, H. Hydrodynamic Investigation of an Oscillating Buoy Wave Energy Converter Integrated into a Pile-restrained Floating Breakwater. *Energies* **2017**, *10*, 712. [CrossRef]
17. Shadman, M.; Estefen, S.F.; Rodriguez, C.A.; Nogueira, I.C. A Geometrical Optimization Method Applied to a Heaving Point Absorber Wave Energy Converter. *Renew. Energy* **2018**, *115*, 533–546. [CrossRef]
18. Reabroy, R.; Zheng, X.; Zhang, L.; Zang, J.; Yuan, Z.; Liu, M.; Sun, K.; Tiaple, Y. Hydrodynamic Response and Power Efficiency Analysis of Heaving Wave Energy Converter Integrated with Breakwater. *Energy Convers. Manag.* **2019**, *195*, 1174–1186. [CrossRef]
19. Zhang, Y.; Li, M.; Zhao, X.; Chen, L. The Effect of the Coastal Reflection on the Performance of a Floating Breakwater-WEC System. *Appl. Ocean Res.* **2020**, *100*, 102117. [CrossRef]
20. Ahmed, A.; Wang, Y.; Azam, A.; Zhang, Z. Design and Analysis of the Bulbous-Bottomed Oscillating Resonant Buoys for an Optimal Point Absorber Wave Energy Converter. *Ocean Eng.* **2022**, *263*, 112443. [CrossRef]
21. He, Z.; Ning, D.; Gou, Y.; Zhou, Z. Wave Energy Converter Optimization Based on Differential Evolution Algorithm. *Energy* **2022**, *246*, 123433. [CrossRef]
22. Nguyen, T.T.D.; Park, J.W.; Yoon, H.K.; Jung, J.C.; Lee, M.M.S. Experimental Study on Application of an Optical Sensor to Measure Mooring-Line Tension in Waves. *J. Ocean Eng. Technol.* **2022**, *36*, 153–160. [CrossRef]

23. Rossell, W.; Ozeren, Y.; Wren, D. Experimental Investigation of a Moored, Circular Pipe Breakwater. *J. Waterw. Port Coast. Ocean Eng.* **2021**, *147*, 04021019. [CrossRef]

24. Guo, W.; Zou, J.; He, M.; Mao, H.; Liu, Y. Comparison of Hydrodynamic Performance of Floating Breakwater with Taut, Slack, and Hybrid Mooring Systems: An SPH-Based Preliminary Investigation. *Ocean Eng.* **2022**, *258*, 111818. [CrossRef]

25. Xu, S.; Wang, S.; Soares, C.G. Review of Mooring Design for Floating Wave Energy Converters. *Renew. Sustain. Energy Rev.* **2019**, *111*, 595–621. [CrossRef]

26. Qiao, D.; Haider, R.; Yan, J.; Ning, D.; Li, B. Review of Wave Energy Converter and Design of Mooring System. *Sustainability* **2020**, *12*, 8251. [CrossRef]

27. Manisha; Kaligatla, R.B.; Sahoo, T. Effect of Bottom Undulation for Mitigating Wave-Induced Forces on a Floating Bridge. *Wave Motion* **2019**, *89*, 166–184. [CrossRef]

28. Vijay, K.G.; Venkateswarlu, V.; Sahoo, T. Bragg Scattering of Surface Gravity Waves by an Array of Submerged Breakwaters and a Floating Dock. *Wave Motion* **2021**, *106*, 102807. [CrossRef]

29. Jiang, L.; Zhang, J.; Tong, L.; Guo, Y.; He, R.; Sun, K. Wave Motion and Seabed Response around a Vertical Structure Sheltered by Submerged Breakwaters with Fabry–Pérot Resonance. *J. Mar. Sci. Eng.* **2022**, *10*, 1797. [CrossRef]

30. Heo, S.; Koo, W.; Kim, M. Optimization Analysis of the Shape and Position of a Submerged Breakwater for Improving Floating Body Stability. *J. Ocean Eng. Technol.* **2024**, *38*, 53–63. [CrossRef]

31. Chen, K.; Zhou, F.; Yin, L.; Wang, S.; Wang, Y.; Wan, F. A Hybrid Particle Swarm Optimizer with Sine Cosine Acceleration Coefficients. *Inf. Sci.* **2018**, *422*, 218–241. [CrossRef]

32. Jeong, H.J.; Koo, W. Analysis of Various Algorithms for Optimizing the Wave Energy Converters Associated with a Sloped Wall-Type Breakwater. *Ocean Eng.* **2023**, *276*, 114199. [CrossRef]

33. Kim, M.H.; Koo, W.C.; Hong, S.Y. Wave interactions with 2D structures on/inside porous seabed by a two-domain boundary element method. *Appl. Ocean Res.* **2000**, *22*, 255–266. [CrossRef]

34. Nakos, D.E. Ship Wave Patterns and Motions by a Three-Dimensional Rankine Panel Method. Ph.D. Thesis, Massachusetts Institute of Technology, Cambridge, MA, USA, 1990.

35. Lee, C.H. *WAMIT Theory Manual. Report No. 95-2*; Department of Ocean Engineering, Massachusetts Institute of Technology: Cambridge, MA, USA, 1995.

36. Folley, M. (Ed.) *Numerical Modelling of Wave Energy Converters: State-of-the-Art Techniques for Single Devices and Arrays*; Academic Press: Cambridge, MA, USA, 2016.

37. Koh, H.J.; Ruy, W.S.; Cho, I.H.; Kweon, H.M. Multi-Objective Optimum Design of a Buoy for the Resonant-Type Wave Energy Converter. *J. Mar. Sci. Technol.* **2015**, *20*, 53–63. [CrossRef]

38. Tom, N.M.; Lawson, M.J.; Yu, Y.H.; Wright, A.D. Development of a Nearshore Oscillating Surge Wave Energy Converter with Variable Geometry. *Renew. Energy* **2016**, *96*, 410–424. [CrossRef]

39. Koley, S.; Panduranga, K.; Almashan, N.; Neelamani, S.; Al-Ragum, A. Numerical and Experimental Modeling of Water Wave Interaction with Rubble Mound Offshore Porous Breakwaters. *Ocean Eng.* **2020**, *218*, 108218. [CrossRef]

40. He, F.; Huang, Z. Hydrodynamic Performance of Pile-Supported OWC-Type Structures as Breakwaters: An Experimental Study. *Ocean Eng.* **2014**, *88*, 618–626. [CrossRef]

41. Goda, Y. A Comparative Review on the Functional Forms of Directional Wave Spectrum. *Coast. Eng. J.* **1999**, *41*, 1–20. [CrossRef]

42. Pastor, J.; Liu, Y. Power Absorption Modeling and Optimization of a Point Absorbing Wave Energy Converter Using Numerical Method. *J. Energy Resour. Technol.* **2014**, *136*, 021207. [CrossRef]

43. Goda, Y. *Random Seas and Design of Maritime Structures*, 3rd ed.; World Scientific Co Pte. Ltd.: Tokyo, Japan, 2010.

44. Eberhart, R.; Kennedy, J. A New Optimizer Using Particle Swarm Theory. In MHS'95. Proceedings of the Sixth International Symposium on Micro Machine and Human Science, Nagoya, Japan, 4–6 October 1995; pp. 39–43.

45. Shami, T.M.; El-Saleh, A.A.; Alswaitti, M.; Al-Tashi, Q.; Summakieh, M.A.; Mirjalili, S. Particle swarm optimization: A comprehensive survey. *IEEE Access* **2022**, *10*, 10031–10061. [CrossRef]

46. Shi, Y.; Eberhart, R.C. Parameter Selection in Particle Swarm Optimization. In Proceedings of the Evolutionary Programming VII: 7th International Conference, EP98, San Diego, CA, USA, 25–27 March 1998; Springer: Berlin/Heidelberg, Germany, 1998; pp. 591–600.

47. Ahandani, M.A. Opposition-Based Learning in the Shuffled Bidirectional Differential Evolution Algorithm. *Swarm Evol. Comput.* **2016**, *26*, 64–85. [CrossRef]

48. Cao, F.; Han, M.; Shi, H.; Li, M.; Liu, Z. Comparative Study on Metaheuristic Algorithms for Optimising Wave Energy Converters. *Ocean Eng.* **2022**, *247*, 110461. [CrossRef]

49. Vugts, J.H. The hydrodynamic coefficients for swaying, heaving, and rolling cylinders in a free surface. *Int. Shipbuild. Prog.* **1968**, *15*, 251–276. [CrossRef]

50. Jeong, W.M.; Oh, S.H.; Ryu, K.H.; Back, J.D.; Choi, I.H. Establishment of Wave Information Network of Korea (WINK). *J. Korean Soc. Coast. Ocean Eng.* **2018**, *30*, 326–336. [CrossRef]

51. WINK. Wave Information Network of Korea (WINK). Available online: http://wink.go.kr/map/map.do (accessed on 4 March 2024).

52. Guth, S.; Katsidoniotaki, E.; Sapsis, T.P. Statistical Modeling of Fully Nonlinear Hydrodynamic Loads on Offshore Wind Turbine Monopile Foundations Using Wave Episodes and Targeted CFD Simulations through Active Sampling. *Wind. Energy* **2024**, *27*, 75–100. [CrossRef]
53. Falnes, J.; Lillebekken, P.M. Budal's latching-controlled-buoy type wave-power plant. In Proceedings of the Fifth European Wave Energy Conference, Cork, Ireland, 17–20 September 2003; pp. 233–244.
54. Katsidoniotaki, E.; Göteman, M. Numerical Modeling of Extreme Wave Interaction with Point-Absorber Using OpenFOAM. *Ocean Eng.* **2022**, *245*, 110268. [CrossRef]
55. Liu, Y.; Yue, D.K. On Generalized Bragg Scattering of Surface Waves by Bottom Ripples. *J. Fluid Mech.* **1998**, *356*, 297–326. [CrossRef]